03,13

# Influence of spark plasma sintering parameters on the thermoelectric properties of n-type $Mg_3Sb_2$-$Mg_3Bi_2$ solid solution materials

© A.A. Mikhailova[1,2], K.A. Shcherbakova[1,2], E.V. Argunov[1], A.A. Markin[2], A.R. Akhmadeev[2], V.A. Dybov[2], M.V. Ananyev[3], N.Yu. Tabachkova[1]

[1] National University of Science and Technology MISiS, Moscow, Russia
[2] Federal State Research and Development Institute of Rare Metal Industry (JSC „Giredmet"), Moscow, Russia
[3] School of Chemical Engineering, University of Birmingham, United Kingdom

E-mail: aluona_mikhailova_style@mail.ru

*Received May 28, 2025*
*Revised September 3, 2025*
*Accepted September 22, 2025*

Samples based on the $Mg_3Sb_2$-$Mg_3Bi_2$ solid solution were obtained by mechanochemical synthesis followed by spark plasma sintering. The regularities of the influence of compaction process parameters on the electrical and thermal physical properties of the samples were identified. It was established that the application of a two-stage heating regime promotes an increase in electrical conductivity up to 325 S/cm at 390 K, while simultaneously ensuring a reduction in lattice thermal conductivity to 0.49 $W/(m \cdot K)$. Collectively, these changes enable achieving a maximum thermoelectric figure of merit $zT$ of 1.38 at 732 K.

**Keywords:** Thermoelectric materials, Zintl phases, Seebeck coefficient, electrical conductivity, thermal conductivity.

DOI: 10.61011/PSS.2025.09.62348.149-25

## 1. Introduction

Thermoelectric generators (TEG) are versatile devices for disposal of waste heat and electric power generation. Presently, in order to manufacture TEGs, tellurides of lead and germanium are used [1], but some thermoelectric materials (TEM) contain environmentally toxic elements, such as lead, cadmium, arsenic, etc., while tellurium and germanium belong to costly elements [2]. In this regard, one of the main tasks is to search for promising TEMs based on environmentally friendly and cheap components.

The main characteristics that determines a TEM quality is a dimensionless figure of merit which is determined by the formula [3]

$$zT = \frac{\alpha^2 \sigma}{\kappa} T, \qquad (1)$$

where $\sigma$, S/cm — conductivity; $\alpha, \mu$V/K — Seebeck coefficient; $\kappa = \kappa_{lat} + \kappa_{el}$ — total thermal conductivity, where $\kappa_{lat}$ and $\kappa_{el}$ — lattice and electron components of thermal conductivity, respectively $W/(m \cdot K)$; $T$ — the absolute temperature, K.

One of the promising mid-temperature TEMs are Zintl phases. The Zintl phases are intermetallic compounds that are formed by alkaline and alkaline earth metals [4–6]and elements of the groups 13−15 of the Periodic table, which form anion clusters.

The interest is recently paid to the TEMs based on the solid solution $Mg_3Sb_2$-$Mg_3Bi_2$, which classically represent the Zintl phase. It is known from the literature data that the material has a high theoretical $zT$ 2.1 at the temperature of 750 K [7]. As compared to other mid-temperature TEMs, the materials based on $Mg_3Sb_2$ are more environmentally-friendly and do not contain costly elements. In its pure form, $Mg_3Sb_2$ has p-type conductance due to a high equilibrium concentration of magnesium vacancies ($V_{Mg}$) [2,8] and has been considered as a promising p-type material with $zT < 1$ [9,10]. In 2016, a group of scientists [11] successfully produced magnesium antimonide of n-type conductance by doping with tellurium and adding excess magnesium that decrease the concentration $V_{Mg}$; the obtained compound had a $zT$ value of 1.5 at 716 K.

The identical hexagonal structure of $Mg_3Sb_2$ and $Mg_3Bi_2$ with the space group of the symmetry $P\bar{3}m1$ allows forming a continuous series of the solid solutions without phase separation [12]. In most cases, when the solid solution is formed, the mobility of charge carriers is reduced due to scattering on a structure disorder. In the solid solution $Mg_3Sb_2$-$Mg_3Bi_2$, the mobility of the charge carriers increases due to a smaller effective mass of electrons of $Mg_3Bi_2$ than in $Mg_3Sb_2$. The average effective mass of electrons is reduced in the solid solution being formed, thereby increasing the mobility and, therefore, conductance. Besides, phonon scattering when substituting antimony with

bismuth reduces thermal conductivity without significantly increasing charge carrier scattering, thereby contributing to preservation of high mobility [11].

Sintering of the powder produced by mechanochemical synthesis (MCS), which is the main method of $Mg_3Sb_2$-$Mg_3Bi_2$ synthesis, is an important step in manufacturing bulk TEMs, since this step includes determination of a direction, a velocity and a temperature of pressing as well as a rate of secondary recrystallization. The pressing step involves forming the microstructure of the bulk TEM, which affects its thermoelectric properties. The compaction process is carried out by such methods as hot pressing (HP) [10,13,14] and spark plasma sintering (SPS) [11,12]. The SPS method is based on simultaneous impact on the material by high-intensity pulsed direct current and uniaxial pressure, wherein the samples are sintered for a short time at a relatively lower temperature as compared to HP thereby making it possible to avoid the grain growth that worsens the thermophysical properties of the material.

Table A1 of Appendix shows literature data of the various modes of sintering of TEMs based on $Mg_3Sb_2$ and values of their. The SPS modes were selected and implemented based on the data studied. The two-step sintering process was studied in the article [15] without describing the microstructure of the produced samples. Moreover (see Table A1 of Appendix), there is no information about comparing two-step and single-stage sintering of the powders of the same composition.

The present study aims to determine the optimal parameters spark plasma sintering of TEMs based on the solid solution $Mg_3Sb_2$-$Mg_3Bi_2$ and studying their influence on the thermoelectric properties.

## 2. Experimental

The samples of the solid solution $Mg_{3.2}Sb_{1.5}Bi_{0.5}$, which were doped with Te and Cu, were fabricated by the MCS method in a planetary ball mill (PBM) Retsch PM 400 MA. The initial components were preliminarily ground in a mortar and after that stoichiometrically placed into a stainless steel ball mill drum in an argon inert atmosphere with addition of (chemically pure) n-hexane as a medium for synthesis. A ratio of the material to stainless steel grinding balls of the diameter from 5 to 15 mm was from 1 : 5 to 1 : 10, respectively. The MCS time was from 3 to 5 h, while the ball mill drum rotational speed was 300–600 rpm. After grinding, hexane was evaporated in a drying oven at the room temperature for 8 h and the obtained powder was sifted in a 250-$\mu$m sieve for separation of agglomerates. The powders were consolidated by the SPS method in an installation SPS-511S (Dr. Sinter Lab., Japan). The produced powder was placed into a graphite press mold of the diameter of 20 mm. It was loaded and unloaded in a glove box in the argon inert atmosphere. The obtained samples were annealed in quartz crucibles for 24 h at the temperature of 400–600 °C in the argon atmosphere to eliminate residual stresses.

In order to measure the properties, samples had been prepared in the form of a cylinder $3\times3\times12\,mm^3$ and a disc of the diameter of 12.6 mm and the thickness of 1.5 mm.

The phase analysis was performed by an X-ray diffraction method using a diffractometer D2 Phaser $CuK_\alpha$ (Bruker, USA). Lattice parameters were refined by the Rietveld method in the Full-Prof software. The microstructure was studied by a method of scanning electron microscopy (SEM) in a microscope Quanta FEG 250 (FEI, USA).

The electric resistance was measured by a four-probe method, and the Seebeck coefficient was simultaneously measured by a differential method. The measurements were performed in the helium atmosphere in a setup ZEM-3 (ULVAC Riko, Japan). Thermal diffusivity was measured by a laser spark method in a setup LFA 457 (Netzsch, Germany) in the argon atmosphere. Specific heat capacity was calculated by the Debye formula in the software program Mathcad 15. The density of the samples was measured using hydrostatic weighing. Thermal conductivity was calculated by the formula [16]

$$œ = D_t C_p d, \tag{2}$$

where $D_t, mm^2/s$ — thermal diffusivity; $C_p, J/(K\cdot kg)$ — specific heat capacity; $d, g\cdot cm^{-3}$ — the density.

Measurement errors of the Seebeck coefficient and conductivity as well as the calculated values of total thermal conductivity were about 5 %. All the measurements were carried out in the temperature range 390–770 K.

## 3. Discussion of results

SPS settings were selected based on analysis of literature data of the compounds of the similar composition, whose basic parameters are given in Table A1 of Appendix. The SPS modes used within the framework of this study and their respective markings are listed in Table 1.

Figure 1 shows diffraction patterns of the powder after MCS and the samples produced at the various SPS modes after annealing.

It follows from the presented results (Figure 1, the curve *0*) that the phase composition of the powder after MCS corresponds to the $\alpha$-phase $Mg_3Sb_2$, peaks from other phases are not observed. The results of the study of the diffraction patterns of the samples at the various sintering modes (Figure 1, the curves *1–6*) have also shown that the diffraction peaks of all the samples correspond to standard data for the $\alpha$- phase $Mg_3Sb_2$, i.e. after SPS and thermal annealing phase transformations do not occur. All the synthesized samples exhibit a predominant grain orientation along the direction ⟨001⟩. In order to quantitatively evaluate the predominant grain orientation, the relative intesities of the peaks of the powder material were calculated. The obtained results are in good agreement with data presented in the study [17]. The sample 60-400-8-800-4 compacted during the two-step sintering (Figure 1, the curve *3*) demonstrates the less pronounced predominant

**Table 1.** SPS modes

| № | Marking, MPa-°C-min | Pressure $P$, MPa | Temperature $T$, °C | Time $t$, min |
|---|---|---|---|---|
| 1 | 50-650-10 | 50 | 650 | 10 |
| 2 | 60-700-5 | 60 | 700 | 5 |
| 3 | 60-400-8-800-4 | 60 | 400, 800 | 8, 4 |
| 4 | 50-800-10 | 50 | 800 | 10 |
| 5 | 45-680-8 | 45 | 680 | 8 |
| 6 | 50-750-5 | 50 | 750 | 5 |

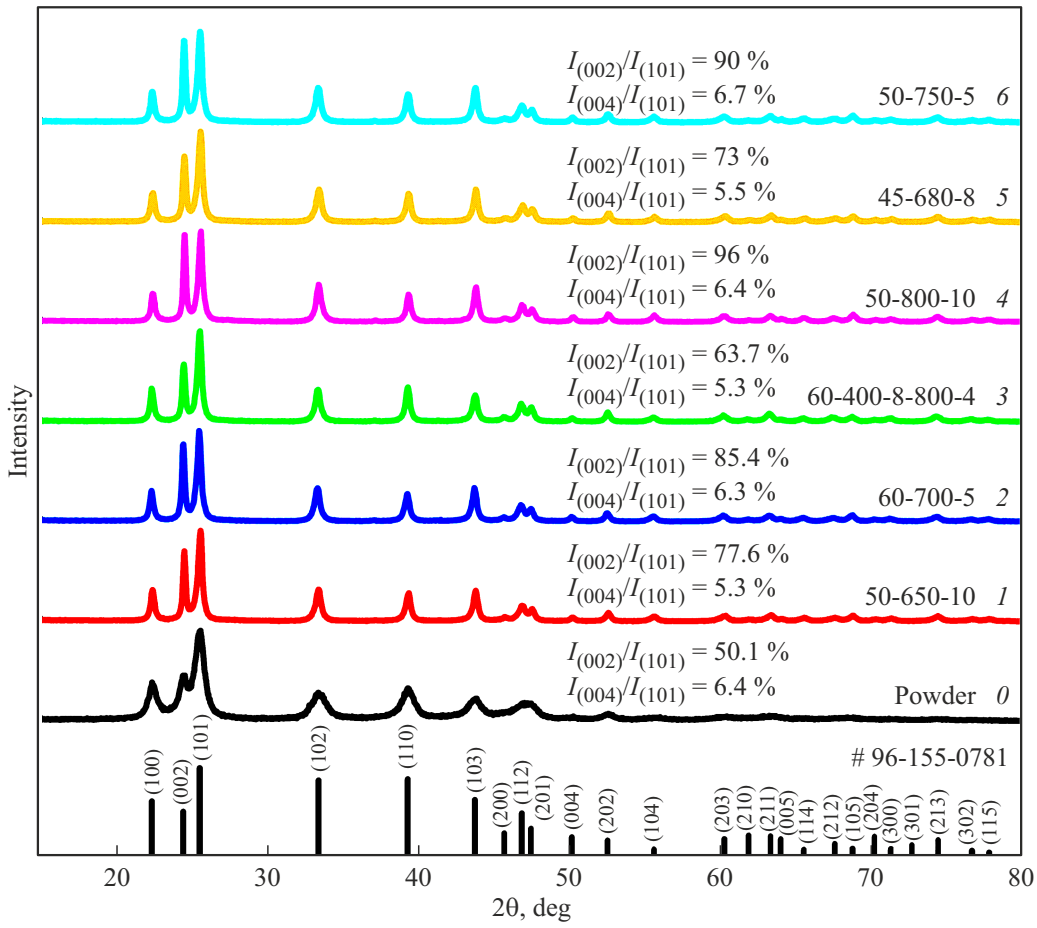


**Figure 1.** Diffraction patterns of the powder after MCS (the curve *0*) and the compacted samples of the solid solution $Mg_3Sb_2$-$Mg_3Bi_2$ (the curves *1*–*6*), which are produced at the various SPS modes.

grain orientation along the direction ⟨001⟩ as compared with other samples produced in the one-step process.

Data of the crystal parameters, the density and the coherent scattering linear characteristics (size) of the produced samples are shown in Table 2.

The data of the crystal lattice parameters, which are calculated by the Rietveld method, agree with the card № 96-155-0781. A difference in the lattice parameters of the synthesized samples is presumably explained by probability of incorporation of copper into the interstitial sites [18] of the crystal lattice of magnesium antimonide, substitution of sites of magnesium itself [19] or by a combination of the described processes. The densities of all the produced samples exceed 97 %. The CSR size of the samples ranges from 27 to 30 nm, which corresponds to the calculation error.

In order to specify the influence of the SPS modes on the microstructure of the obtained samples, the chips of the samples were studied by the SEM method. The images of the chips of the produced samples are shown in Figure 2.

It follows from the analysis of the microstructure of the chips of the samples that the size of grain agglomerates of the samples in Figure 2, *a, b, e* and *f* is equal to several

**Table 2.** Crystal structure parameters $a$ and $c$, the density $d$, the relative density $d_r$ and CSR ($D_{CSR}$) of the produced samples

| Marking, MPa-°C-min | $a$, Å | $c$, Å | $d$, g/cm$^3$ | $d_r$, % | $D_{CSR}$, nm |
|---|---|---|---|---|---|
| 50-650-10 | 4.583 | 7.273 | 4.403 | 97.7 | 29 |
| 60-700-5 | 4.587 | 7.280 | 4.377 | 97.1 | 30 |
| 60-400-8-800-4 | 4.580 | 7.266 | 4.381 | 97.2 | 28 |
| 50-800-10 | 4.587 | 7.279 | 4.391 | 97.4 | 30 |
| 45-680-8 | 4.587 | 7.278 | 4.402 | 97.6 | 27 |
| 50-750-5 | 4.585 | 7.274 | 4.398 | 97.6 | 29 |

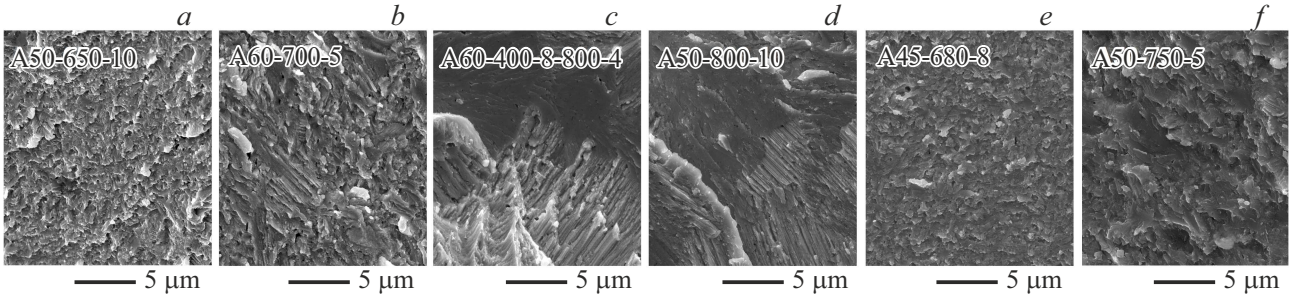


**Figure 2.** SEM images of chips of the samples of the solid solution $Mg_3Sb_2$-$Mg_3Bi_2$, which are fabricated at the various SPS modes.

micrometers (sintering at 650−750 °C), while two other samples in Figure 2, *c* and *d* have the size of tens of micrometers (sintering at 800 °C). The morphology and microstructure of the chips of the samples were analyzed to detect a direct dependence of their structure on the sintering temperature. For the samples sintered within the range 650−750 °C, the microstructure evolves from a uniform equiaxed one at 650−680 °C to a coarsened, homogeneous and lamellar one at 750 °C. A fundamental change is observed at 800 °C, where a columnar structure is formed. This structure is not detected at the lower temperatures, which can be explained by an effect of liquid phase sintering occurring at higher temperatures [20], which promotes formation of a major and anisotropic grain. The columnar structure leads to an increase of conductance of the material along the predominant direction due to an increase of the mean free path [21]

Element mapping shows that there is heterogeneous distribution observed for the samples 50-650-10 and 50-750-5. The samples with the SPS modes 60-700-5 and 45-680-8 have more uniform distribution of the elements, but there are surface defects. The samples with the SPS modes 60-400-8-800-4 and 50-800-10 are characterized by uniform distribution and a homogeneous surface.

Therefore, the samples with the SPS modes 60-400-8-800-4 and 50-800-10, which are characterized by the columnar structure, predominant orientation of grains along the direction ⟨001⟩ as well as by the most uniform distribution of the elements are selected for further study of the thermoelectric properties.

Figure 3, *a* demonstrates a temperature dependence of conductivity $\sigma$ of the two studied samples. Within the temperature range 373−500 K, the sample 50-800-10 exhibits a semiconductor nature of conductance with the maximum of 250 S/cm at 473 K, whereas the sample 60-400-8-800-4 demonstrates a metallic behavior. At the temperatures above 500 K, the dependences $\sigma$ for both samples become identical, decreasing almost linearly with the increase of the temperature, which corresponds to the metallic type of conductance.

Figure 3, *b* shows a temperature dependence of the Seebeck coefficient $\alpha$. Within the studied temperature range, the values of $\alpha$ for both samples demonstrate a similar type of behaviour, varying within the interval from $-200$ to $-280\,\mu$V/K. We observed an almost linear increase of the absolute value of the Seebeck coefficient with the increase of the temperature. This dependence agrees with a typical behavior of metals or degenerate semiconductors, in which charge carrier scattering on acoustic phonons prevails.

Figure 3, *c* shows a temperature dependence of the power factor ($PF = S^2\sigma$) of the studied samples. The data are analyzed to show an advantage of the two-step sintering mode: the sample 60-400-8-800-4 demonstrates higher values of $PF$ as compared to the single-stage sample 50-800-10 within the entire studied temperature range. The obtained values are induced by a synergistic effect of electrophysical characteristics. The maximum values of the power factor are achieved at 504 K and are equal to $15.2\,\mu\text{W}/(\text{cm}\cdot\text{K}^2)$ for the two-step sample and $13.2\,\mu\text{W}/(\text{cm}\cdot\text{K}^2)$ for the single-step.

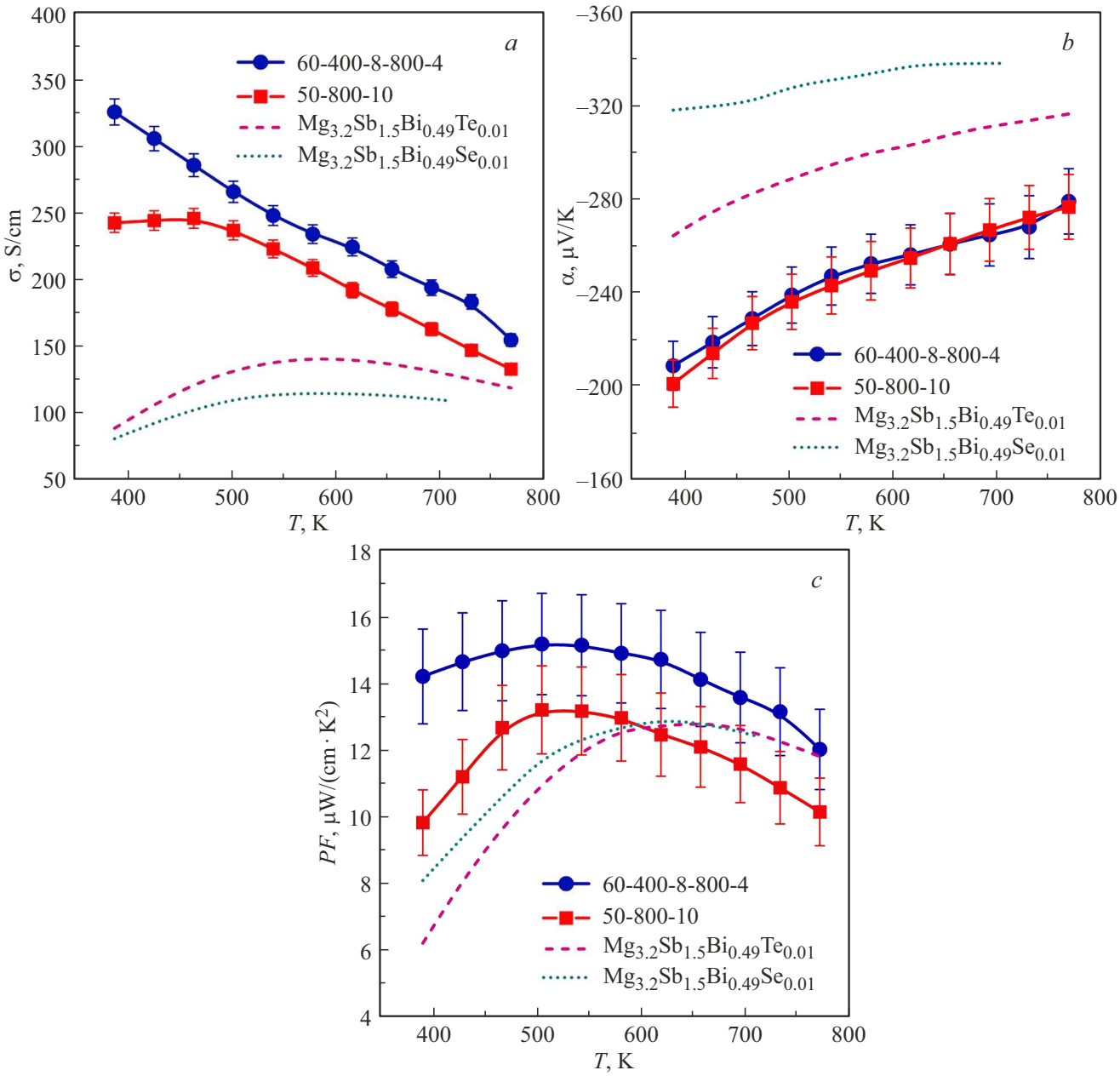


**Figure 3.** Temperature dependences of *a*) conductivity, *b*) the Seebeck coefficient and *c*) the power factor of the samples of the solid solution $Mg_3Sb_2$-$Mg_3Bi_2$ are shown by solid lines. The literature data [19,22] are shown by dashed lines.

Figure 4, *a* shows a temperature dependence of the total thermal conductivity of the studied samples. The measured values of $\kappa$ for all the samples vary within the range $0.67-0.97\,\mathrm{W/(m\cdot K)}$, which corresponds to ultra-low thermal conductivity within the studied temperature range. The temperature dependence is analysed to demonstrate the qualitative similarity between the thermal conductivity behaviour of the experimental samples and the data from the studies [19,22], which is manifested in the same slope of the temperature curves $\kappa(T)$. This coincidence may indicate similar mechanisms of heat transfer in these materials.

Figure 4, *b* shows data of the electron thermal conductivity of the studied samples. The results are analyzed to show that the single-step sample demonstrates the value of $\kappa_{el}$ that are lower than the values of the sample produced by the two-step method. The obtained result is caused by the fact that the electron component of the thermal conductivity is directly proportional to the electrical conductivity via the Wiedemann–Franz law:

$$\frac{\kappa_e}{\sigma} = LT, \tag{3}$$

where $L, 10^{-8}\mathrm{W\Omega K^{-2}}$ is a Lorentz number calculated by an empirical expression [23]:

$$L = 1.5 + \exp\left(-\frac{|S|}{116}\right). \tag{4}$$

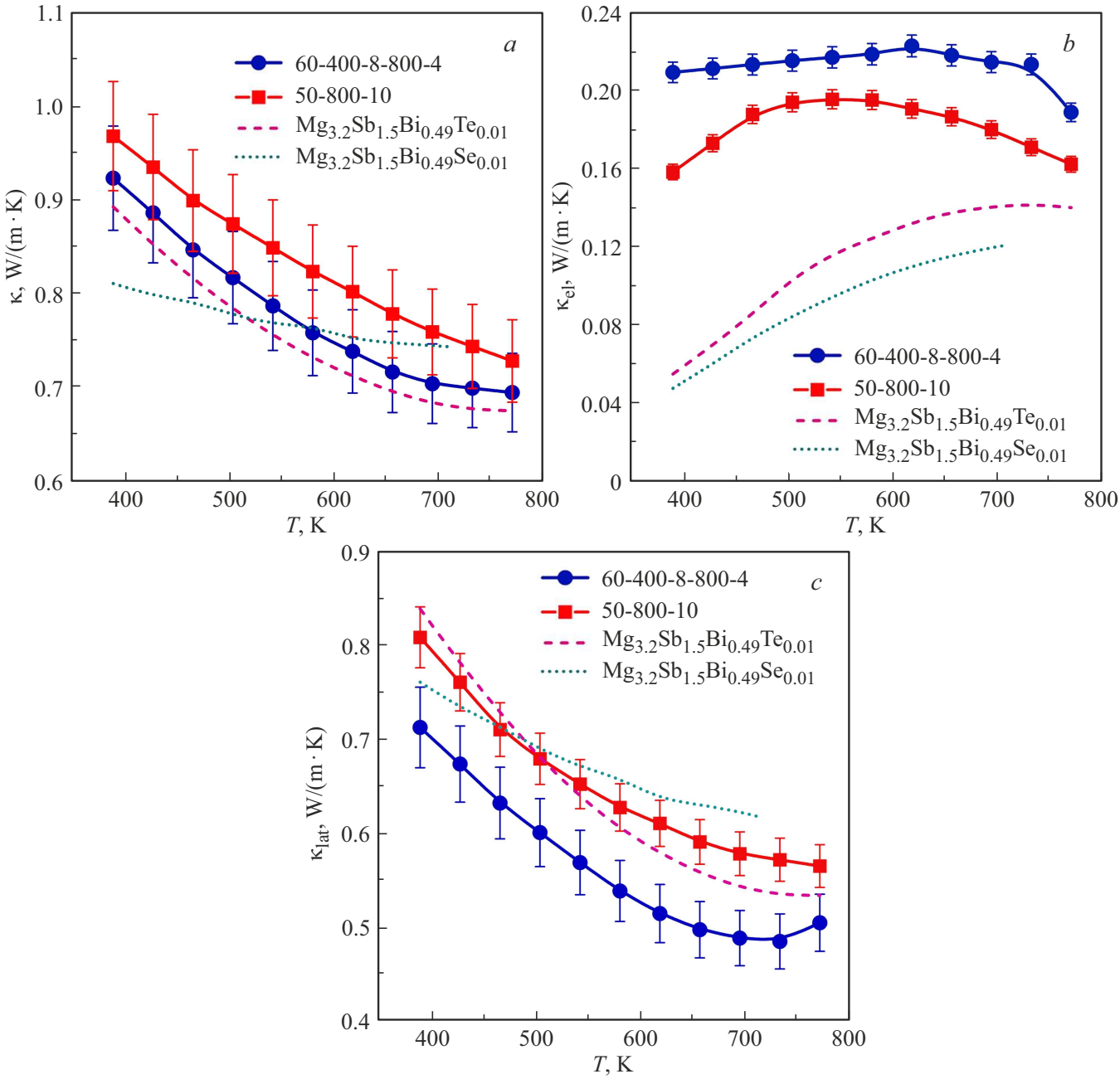


**Figure 4.** Temperature dependences of *a*) total; *b*) electron and *c*) lattice thermal conductivities of the samples of the solid solution $Mg_3Sb_2$-$Mg_3Bi_2$ are shown by solid lines. The literature data [19,22] are shown by dashed lines.

Figure 4, *c* shows a temperature dependence of lattice thermal conductivity of the studied samples. The sample 60-400-8-800-4 demonstrates a non-monotonic behavior of $\kappa_{lat}(T)$: an initial decrease of the thermal conductivity in the low-temperature range is replaced by its increase with the increase of the temperature. Such behavior can be explained by competition of two mechanisms: domination of phonon scattering at the low temperatures, which results in a decrease of $\kappa_{lat}$, and activation of bipolar diffusion at the higher temperatures, which causes the increase of thermal conductivity. Unlike it, the sample 50-800-10 shows a traditional monotonic decrease of the lattice thermal conductivity with the increase of the temperature within the entire studied range.

Figure 5 shows temperature dependences of A $zT$ for the studied samples. The single-step sample has the values of $zT$ within the range 0.4–1.1 within the entire studied temperature range. In contrast, the two-step sample reaches the maximum value $zT = 1.38$ at 732 K, which is significant improvement of the thermoelectric characteristics. A dimensionless figure of merit is improved due to the synergistic effect: first of all, by optimizing conductance,

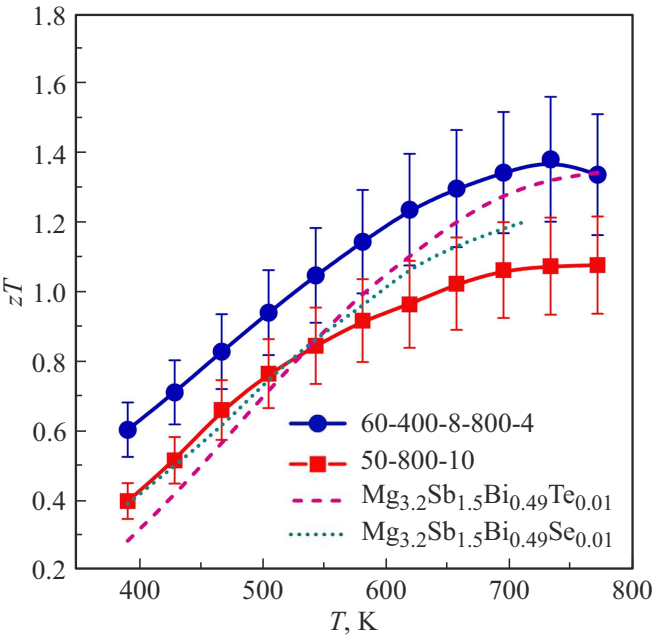


**Figure 5.** Temperature dependences of the thermoelectric Q factor for the samples of the solid solution $Mg_3Sb_2$-$Mg_3Bi_2$ are shown by solid lines. The literature data [19,22] are shown by dashed lines.

and secondly, by suppressing the phonon component of thermal conductivity. The transport properties are optimised by selecting the compaction parameters, including the temperature and sintering duration, in a rational manner. The obtained results demonstrate efficiency of using the two-step synthesis for improving the thermoelectric characteristics of the material.

## 4. Conclusions

The method of mechanochemical synthesis with subsequent spark plasma sintering was used to obtain the single-phase thermoelectric material based on the solid solution $Mg_3Sb_2$-$Mg_3Bi_2$. The microstructure characteristics of the samples synthesized at the various sintering modes were comprehensively analyzed to find optimal conditions of formation of the material.

The following specified dependence is crucial: applying the two-step sintering mode makes it possible to increase conductance of the material with simultaneous reduction of the lattice component of thermal conductivity, which is achieved by suppressing the grain growth, optimizing the defect structure and controlling a phonon scattering spectrum.

The performed optimization resulted in achieving the value of $zT = 1.38$ at 732 K for the studied system $Mg_3Sb_2$-$Mg_3Bi_2$. The obtained results demonstrate that the developed synthesis procedure is promising for creating highly-efficient thermoelectric materials of this type.

### Acknowledgments

The team of the authors would like to thank B.R. Senatulin, I.V. Chepkasov, M.Yu. Shtern and M.A. Seredina for assistance in conducting the experiments and for discussing the obtained results.

### Conflict of interest

The authors declare that they have no conflict of interest to be disclosed in the present article.

## References

[1] G.J. Snyder, E.S. Toberer. Nature Mater. **7**, *2*, 105 (2008).
[2] Novel Thermoelectric Materials and Device Design Concepts / Eds S. Skipidarov, M. Nikitin. Springer Nature Switzerland AG, Cham (2019). 327 p.
[3] A.F. Ioffe. Poluprovodnikovye termoelementy. Izd-vo AN SSSR, M.-L. (in Russian) (1956).
[4] S.M. Kauzlarich, S.R. Brown, G.J. Snyder. Dalton Trans. *21*, 2099 (2007).
[5] R. Nesper. Prog. Solid State Chem. **20**, *1*, 1 (1990).
[6] Chemistry, Structure, and Bonding of Zintl Phases and Ions / Ed. S.M. Kauzlarich. VCH Publishers, Inc., New York. (1996). 340 p.
[7] F. Meng, S. Sun, J. Ma, C. Chronister, J. He, W. Li. Mater. Today Phys. **13**, 100217 (2020).
[8] S. Ohno, K. Imasato, S. Anand, H. Tamaki, S.D. Kang, P. Gorai, H.K. Sato, E.S. Toberer, T. Kanno, G.J. Snyder. Joule **2**, *1*, 141 (2018).
[9] C. Chen, X. Li, S. Li, X. Wang, Z. Zhang, J. Sui, F. Cao, X. Liu, Q. Zhang. J. Mater. Sci. **53**, *23*, 16001 (2018).
[10] J. Shuai, Y. Wang, H.S. Kim, Z. Liu, J. Sun, S. Chen, J. Sui, Z. Ren. Acta Materialia **93**, 187 (2015).
[11] H. Tamaki, H.K. Sato, T. Kanno. Adv. Mater. **28**, *46*, 10182 (2016).
[12] J. Zhang, L. Song, S.H. Pedersen, H. Yin, T.-H. Le, B.B. Iversen. Nature Commun. **8**, *1*, 13901 (2017).
[13] J. Zhang, L. Song, B.B. Iversen. ACS Appl. Mater. Interfaces. **13**, *9*, 10964 (2021).
[14] M. Wood, J.J. Kuo, K. Imasato, G.J. Snyder. Adv. Mater. **31**, *35*, 1902337 (2019).
[15] Y. Wang, X. Zhang, Y. Liu, Y. Wang, H. Liu, J. Zhang. J. Materiomics **6**, *1*, 216 (2020).
[16] H. Shang, Z. Liang, C. Xu, S. Song, D. Huang, H. Gu, J. Mao, Z. Ren, F. Ding. Acta Materialia **201**, 572 (2020).
[17] L. Hu, Q. Zhang, Z. Shan, L. Wang, Y. Zheng, J. Fan. Scripta Materialia **235**, 115629 (2023).
[18] P. Gorai, B.R. Ortiz, E.S. Toberer, V. Stevanović. J. Mater. Chem. A **6**, *28*, 13806 (2018).
[19] X. Yang, H. Ni, X. Yu, B. Cao, J. Xing, Q. Chen, L. Xi, J. Liu, J. Zhang, K. Guo, J.-T. Zhao. J. Materiomics **10**, *1*, 154 (2024).
[20] M.D. Mikhailov. Sovremennye problemy materialovedeniya nanokompozitnye materialy. Izd-vo Politekhn. un-ta, SPb (2010). (in Russian).
[21] K.V. Shalimova. Fizika poluprovodnikov. Energoatomizdat, M. (1985). 392 s. (in Russian).
[22] L. Yu, W. Li, Z. Zhang, S. Wei, J. Li, Z. Ji, J. Zhuo, G. Lu, W. Song, S. Zheng. Mater. Today Phys. **26**, 100721 (2022).
[23] H.-S. Kim, Z.M. Gibbs, Y. Tang, H. Wang, G.J. Snyder. Appl. Mater. **3**, *4*, 041506 (2015).

# Appendix

**Table A1.** Literature data on the SPS modes for the materials based on $Mg_3Sb_2$

| № | Compound | $T$, K | $P$, MPa | $t$, min | $zT_{max}$ | $T_{max}$, K | Ref. |
|---|---|---|---|---|---|---|---|
| 1 | $Mg_{3.2}Sb_{1.99}Te_{0.01}$ | 953 | 50 | 8 | 0.78 | 773 | [1] |
| 2 | $Mg_{3.17}Y_{0.03}Sb_2$ | 953 | 50 | No data | 0.83 | 773 | [2] |
| 3 | $Mg_{3.5}Gd_{0.04}Sb_{1.97}Te_{0.03}$ | 673 | 60 | 10 | 1.33 | 725 | [3] |
| | $Mg_{3.5}Ho_{0.04}Sb_{1.97}Te_{0.03}$ | 1073 | | 4 | 1.11 | | |
| 4 | $Mg_{3.185}Co_{0.015}(Sb_{0.3}Bi_{0.7})_{1.99}Te_{0.01}$ | 723 | 50 | 10 | 1.03 | 525 | [4] |
| 5 | $Mg_3Sb_{1.8}Bi_{0.2}$ | 1073 | 50 | 10 | 0.60 | 750 | [5] |
| 6 | $Mg_{3.2}Nd_{0.03}Sb_{1.5}Bi_{0.5}$ | 923 | 50 | 5 | 1.8 | 725 | [6] |
| 7 | $Mg_{3.2}Sb_{1.5}Bi_{0.49}Se_{0.01}$ | 923 | 50 | 5 | 1.21 | 723 | [7] |
| | $Mg_{3.18}Pr_{0.02}Sb_{1.5}Bi_{0.49}Se_{0.01}$ | | | | 1.67 | | |
| | $Mg_{3.18}Nd_{0.02}Sb_{1.5}Bi_{0.49}Se_{0.01}$ | | | | 1.74 | | |
| 8 | $Mg_3Sb_{1.97}La_{0.03}$ | 973 | 40 | 15 | 0.93 | 770 | [8] |
| | $Mg_3Sb_{1.95}Sc_{0.05}$ | | | | 0.80 | | |
| 9 | $Mg_3Sb_{1.95}Te_{0.05}$ | 973 | 40 | 15 | $\sim 1.0$ | 768 | [9] |
| 10 | $Mg_{3.2}Sb_{1.5}Bi_{0.49}Te_{0.01}Cu_{0.01}$ | 973 | 60 | 5 | 1.9 | 773 | [10] |
| 11 | $Mg_{3.24}Sb_{1.5}Bi_{0.49}Te_{0.01}$ | 1023 | 45 | 15 | $\sim 1.71$ | 773 | [11] |
| 12 | $Mg_{3.2}In_{0.005}Sb_{1.5}Bi_{0.49}Te_{0.01}$ | 973 | 60 | 20 | $\sim 2.0$ | 723 | [12] |

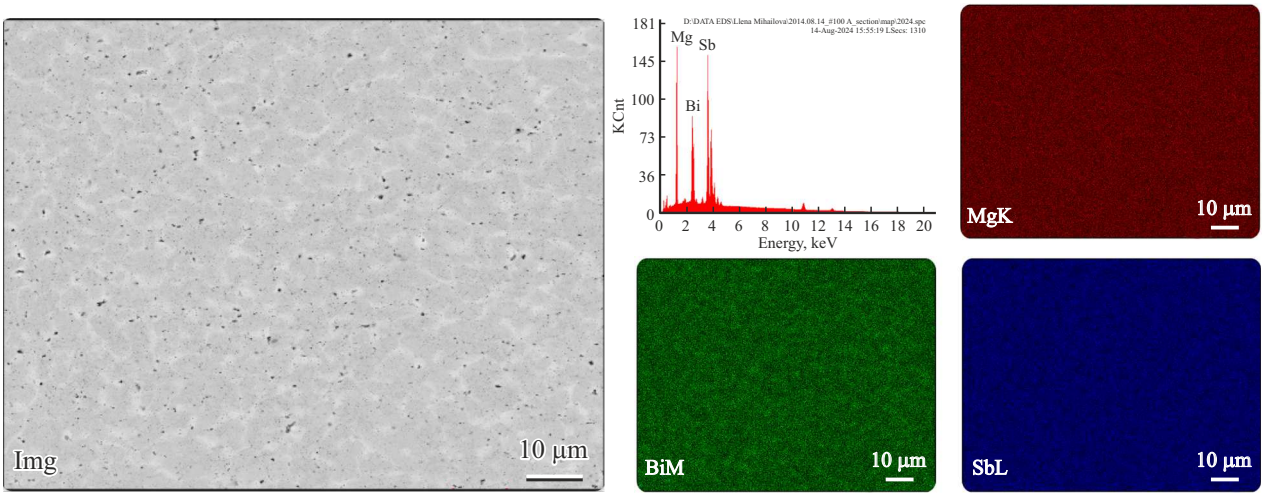


**Figure A.1.** Result of elemental analysis of the surface of the sample with the SPS mode (50-650-10) in SEM.

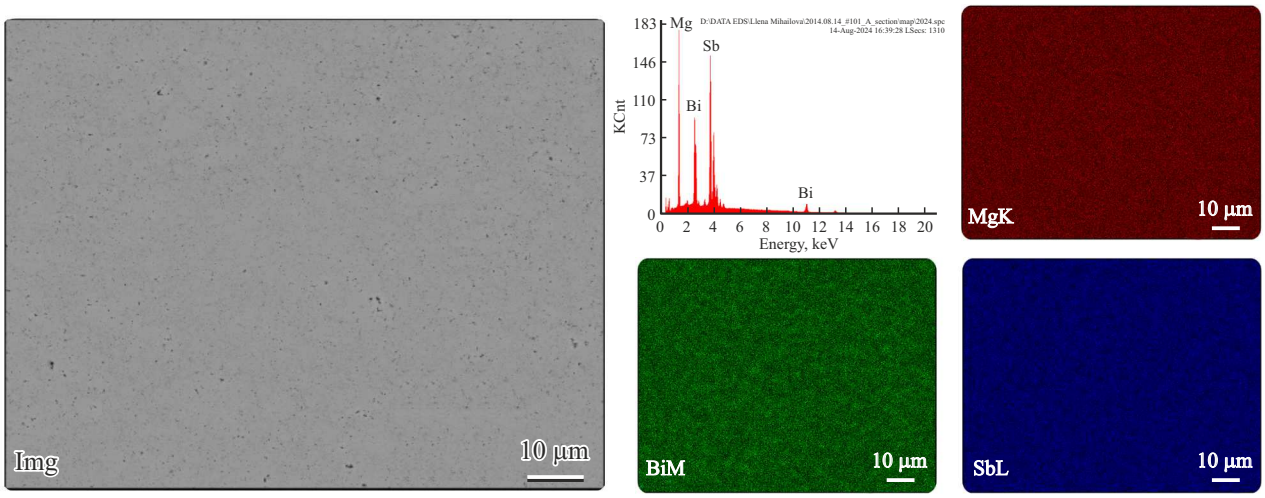


**Figure A.2.** Result of elemental analysis of the surface of the sample with the SPS mode (60-700-5) in SEM.

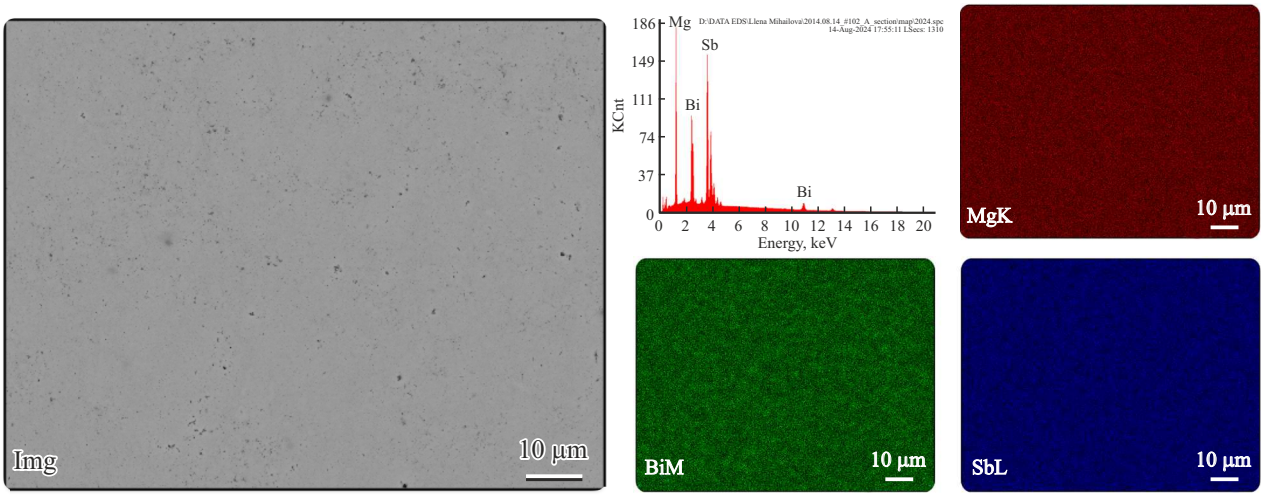


**Figure A.3.** Result of elemental analysis of the surface of the sample with the SPS mode (60-400-8-800-4) in SEM.

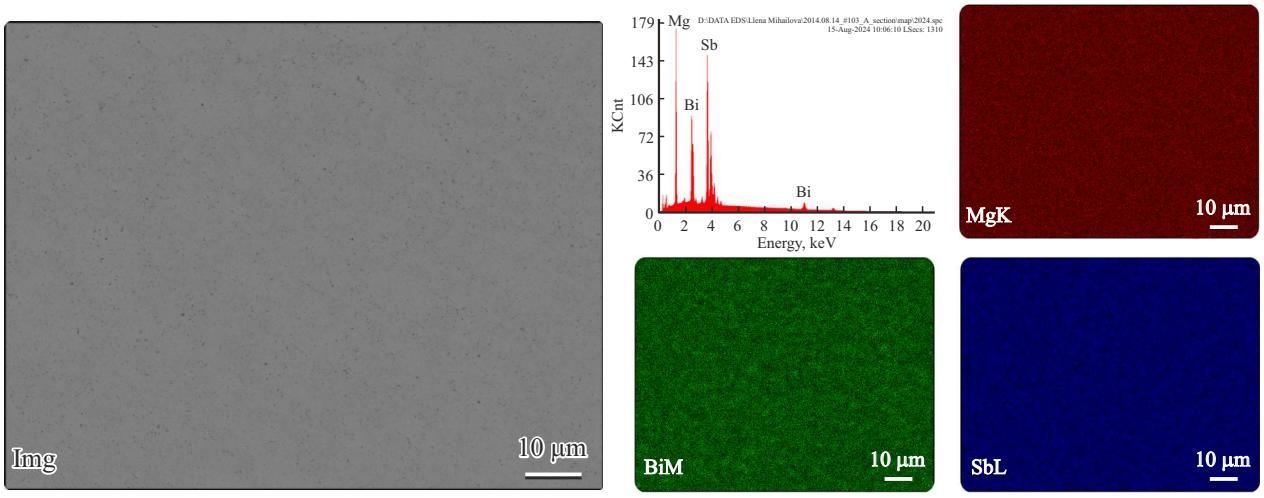


**Figure A.4.** Result of elemental analysis of the surface of the sample with the SPS mode (50-800-10) in SEM.

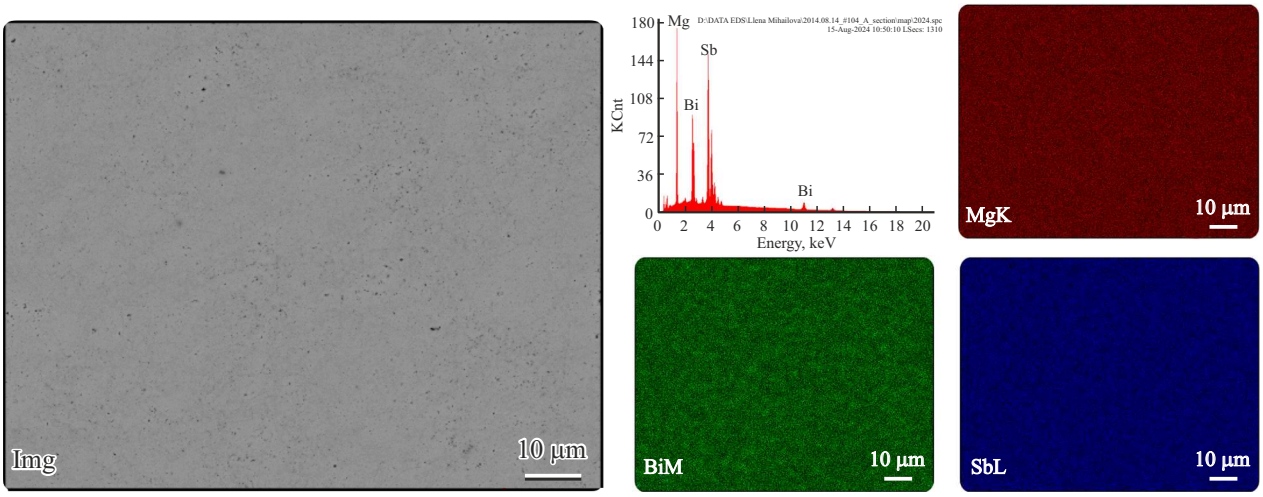


**Figure A.5.** Result of elemental analysis of the surface of the sample with the SPS mode (45-680-8) in SEM.

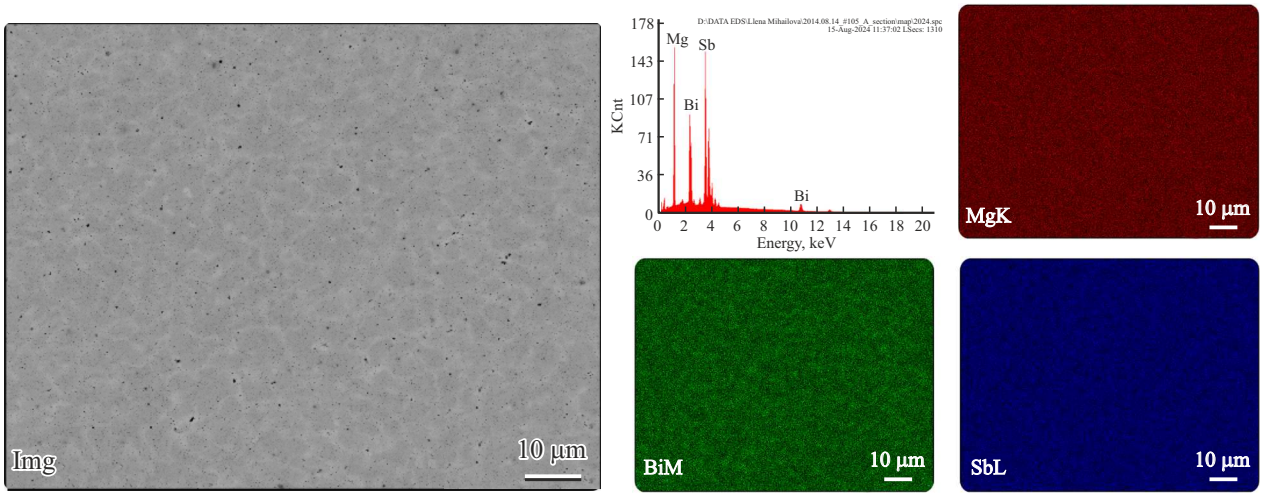


**Figure A.6.** Result of elemental analysis of the surface of the sample with the SPS mode (50-750-5) in SEM.

## Additional list of references

[1] Y. Wang, X. Zhang, Y. Wang, H. Liu, J. Zhang. Phys. Status Solidi A **216**, *6*, 1800811 (2019).
[2] Y. Wang, X. Zhang, Y. Liu, Y. Wang, H. Liu, J. Zhang. J. Materiomics **6**, *1*, 216 (2020).
[3] J. Zhang, L. Song, B.B. Iversen. ACS Appl. Mater. Interfaces. **13**, *9*, 10964 (2021).
[4] Y. Chen, C. Wang, Z. Ma, L. Li, S. Li, J. Wang. Curr. Appl. Phys. **21**, 25 (2021).
[5] A. Bhardwaj, A. Rajput, A.K. Shukla, J.J. Pulikkotil, A.K. Srivastava, A. Dhar, G. Gupta, S. Auluck, D.K. Misra, R.C. Budhani. RSC Adv. **3**, *22*, 8504 (2013).
[6] J. Li, S. Zhang, F. Jia, S. Zheng, X. Shi, D. Jiang, S. Wang, G. Lu, L. Wu, Z.-G. Chen. Mater. Today Phys. **15**, 100269 (2020).
[7] L. Yu, W. Li, Z. Zhang, S. Wei, J. Li, Z. Ji, J. Zhuo, G. Lu, W. Song, S. Zheng. Mater. Today Phys. **26**, 100721 (2022).
[8] J. Tani, H. Ishikawa. J. Mater. Sci.: Mater. Electron. **31**, *10*, 7724 (2020).
[9] J. Tani, H. Ishikawa. Phys. B: Condens. Matter **588**, 412173 (2020).
[10] Z. Liu, N. Sato, W. Gao, J. Yi, K. Yubuta, N. Kawamoto, M. Mitome, K. Kurashima, Y. Owada, K. Nagase, C.-H. Lee, J. Yi, K. Tsuchiya, T. Mori. Joule **5**, *5*, 1196 (2021).
[11] L. Hu, Q. Zhang, Z. Shan, L. Wang, Y. Zheng, J. Fan. Scripta Materialia **235**, 115629 (2023).
[12] L. Wang, W. Zhang, S.Y. Back, N. Kawamoto, D.H. Nguyen, T. Mori. Nature Commun. **15**, *1*, 6800 (2024).

*Translated by M.Shevelev*